

A complex choreography of cell movements shapes the vertebrate eye

Kristen M. Kwan^{1,*}, Hideo Otsuna^{1,*}, Hinako Kidokoro¹, Keith R. Carney², Yukio Saijoh^{1,3} and Chi-Bin Chien^{1,4,*}

SUMMARY

Optic cup morphogenesis (OCM) generates the basic structure of the vertebrate eye. Although it is commonly depicted as a series of epithelial sheet folding events, this does not represent an empirically supported model. Here, we combine four-dimensional imaging with custom cell tracking software and photoactivatable fluorophore labeling to determine the cellular dynamics underlying OCM in zebrafish. Although cell division contributes to growth, we find it dispensable for eye formation. OCM depends instead on a complex set of cell movements coordinated between the prospective neural retina, retinal pigmented epithelium (RPE) and lens. Optic vesicle evagination persists for longer than expected; cells move in a pinwheel pattern during optic vesicle elongation and retinal precursors involute around the rim of the invaginating optic cup. We identify unanticipated movements, particularly of central and peripheral retina, RPE and lens. From cell tracking data, we generate retina, RPE and lens subdomain fate maps, which reveal novel adjacencies that might determine corresponding developmental signaling events. Finally, we find that similar movements also occur during chick eye morphogenesis, suggesting that the underlying choreography is conserved among vertebrates.

KEY WORDS: Zebrafish, Eye, Morphogenesis, Cell tracking, Retina, Retinal pigmented epithelium (RPE), Lens, Fate map

INTRODUCTION

Organogenesis depends on an interplay between patterning and morphogenesis. In a dynamic tissue, such as the developing eye, cell movements can both control and be controlled by patterning. Despite extensive studies of developmental eye patterning (reviewed by Adler and Canto-Soler, 2007; Fuhrmann, 2010; Lang, 2004; Martinez-Morales et al., 2004), the accompanying cell movements have remained largely unstudied.

Previous understanding of optic cup morphogenesis (OCM) comes from fixed tissue analysis (Hilfer, 1983; Hilfer et al., 1981; Li et al., 2000; Schmitt and Dowling, 1994; Schook, 1980a; Schook, 1980b; Silver, 1981). The mature optic cup (OC) comprises neural retina (NR), retinal pigmented epithelium (RPE) and lens. OCM can be divided into four steps (Fig. 1A): evagination, elongation, invagination and rotation. Evagination initially generates a simple pouch on the side of the brain. The optic vesicle (OV) then elongates, and a furrow constricts the connection between eye and brain, forming the optic stalk. During invagination, the NR and RPE enwrap the lens as it emerges from the overlying ectoderm. Once the lens has pinched off from the ectoderm, OCM is considered to be complete. Shortly thereafter, postmitotic retinal neuron differentiation begins. Cellular

mechanisms responsible for OCM have not been determined: although OCM is often depicted as a sequence of epithelial sheet folding events, this lacks any empirical underpinning.

Four cellular mechanisms determine tissue shape: cell division, death, shape change and movement. There is some knowledge of their roles in OCM. In chick, localized proliferation was controversially proposed to underlie certain steps (Hilfer et al., 1981; Schook, 1980a; Silver, 1981). In *Xenopus*, inhibiting proliferation leads to disorganized yet functional eyes, but the time point of OCM completion was not analyzed (Harris and Hartenstein, 1991); it is possible that disorganization arose during OCM rather than subsequently during retinal neurogenesis. In zebrafish, the role of proliferation has not been tested. Cell death has been reported to occur in spatiotemporally regulated patterns during amphibian, chick, mouse and rat OCM (Laemle et al., 1999; Martin-Partido et al., 1988; Schook, 1980a; Schook, 1980b; Silver and Hughes, 1973; Trousse et al., 2001); however, during zebrafish OCM, apoptosis is rare (Cole and Ross, 2001) and therefore cell death is unlikely to play a significant role. Cell movements during OCM have been explored to some degree by fate mapping in chick, *Xenopus* and zebrafish (Dutting and Thanos, 1995; Holt, 1980; Kozlowski et al., 1997; Li et al., 2000; Woo and Fraser, 1995), but with little detailed analysis of OCM, or of RPE and lens.

More recently, in toto imaging and automated cell tracking were used to study cell movements underlying evagination (England et al., 2006; Rembold et al., 2006). Both studies identified novel cell movements and behaviors. OV cell movement is integrated with neighboring telencephalic and hypothalamic brain regions to coordinate forebrain neurulation and early evagination; mutant analysis revealed multiple mechanisms underlying cyclopia (England et al., 2006). Novel subdivisions of the early eye field behave in distinct manners to initiate OV evagination, with a first event being slowed midline convergence of future lateral OV cells (Rembold et al., 2006). Subsequently, it was shown that OV-specific downregulation of the cell adhesion molecule Nlcam

¹Department of Neurobiology and Anatomy, ²Cell Imaging Core, ³Program in Human Molecular Biology and Genetics, and ⁴Brain Institute, University of Utah, Salt Lake City, UT 84132, USA.

*These authors contributed equally to this work

†Authors for correspondence (kristen.kwan@neuro.utah.edu; chi-bin.chien@neuro.utah.edu)

This is an Open Access article distributed under the terms of the Creative Commons Attribution Non-Commercial Share Alike License (<http://creativecommons.org/licenses/by-nc-sa/3.0>), which permits unrestricted non-commercial use, distribution and reproduction in any medium provided that the original work is properly cited and all further distributions of the work or adaptation are subject to the same Creative Commons License terms.

mediates the slowed convergence (Brown et al., 2010). These highly informative studies, however, did not extend beyond initial eye morphogenesis stages.

Many signaling pathways have been implicated in specific OV patterning events, and mutations in these pathways can lead to morphogenetic defects. In zebrafish, FGF signaling patterns the anterior-posterior (AP) axis of the eye, and recent work revealed that patterning is integrated with the regulation of specific cell movements and epithelial cell cohesion (Picker and Brand, 2005; Picker et al., 2009). The zebrafish *patched 2* mutant *blowout* exhibits upregulated Hedgehog pathway activity and coloboma, which is the defective closure of the choroid fissure (Lee et al., 2008). Mouse *Hes1* knockouts exhibit failure of OC invagination and coloboma; this function during OCM may be independent of Notch signaling (Lee et al., 2005; Tomita et al., 1996). The mouse *Lrp6* insertional mutant displays microphthalmia and coloboma, implicating the involvement of canonical Wnt signaling (Pinson et al., 2000; Zhou et al., 2008). Finally, inhibiting retinoic acid signaling in zebrafish and mouse also leads to invagination defects and coloboma (Lupo et al., 2011; Mic et al., 2004).

Cell-intrinsic mechanisms also regulate OCM: the medaka gene *ojoplano* appears to mediate basal constriction underlying invagination (Martinez-Morales et al., 2009). In addition, mouse ES cells grown under specific conditions can differentiate and self-organize into an OC structure without extraocular tissues (Eiraku et al., 2011). Clearly, however, intrinsic mechanisms must be coordinated with extrinsic signals in the embryo. Despite a growing body of work, we lack a comprehensive understanding of OCM and how morphogenetic defects arise.

We aimed here to gain a detailed understanding of the cellular events during vertebrate OCM. Does proliferation contribute to the basic morphogenetic program? When and where do cells move? Are movements temporally and spatially coordinated between retina, RPE and lens?

The optical accessibility of zebrafish embryos offered a unique opportunity to investigate OCM using 4D time-lapse imaging and cell tracking. We analyzed the contributions to OCM of cell division and cell movement, and mapped cell movements and generated fate maps for the component tissues of the eye. Our results identify novel morphogenetic events shaping the retina, RPE and lens, with important implications for their specification, and include studies of OCM in the chick embryo that indicate that this process is conserved across vertebrates.

MATERIALS AND METHODS

Zebrafish

Embryos (Tü or TL strains) were raised at 28.5–30°C and staged according to hours post-fertilization (hpf) and morphology (Kimmel et al., 1995).

RNA synthesis and injections

Capped RNA was synthesized using pCS2 templates (pCS2-EGFP-CAAX, pCS2FA-H2A.F/Z-mCherry, pCS2FA-Kaede, pCS2FA-nls-Kaede) and the mMessage mMachine SP6 Kit (Ambion), purified (Qiagen RNeasy Mini Kit) and ethanol precipitated; 300–500 pg RNA was injected into one-cell embryos.

Cell cycle inhibition

Embryos (10.5 hpf) were dechorionated and incubated in E3 (untreated), DMSO control (E3 containing 3% DMSO) or HUA (E3 containing 20 mM hydroxyurea, 150 μ M aphidicolin, 3% DMSO) (Lyons et al., 2005). Embryos (24 hpf) were fixed in 4% paraformaldehyde (PFA), permeabilized in TBST (TBS containing 0.1% Triton X-100), blocked in TBST containing 2% BSA and incubated with anti-phospho-histone H3 antibody (1:250; Millipore, 06-570), then goat anti-rabbit secondary

antibody (Invitrogen, A-11008) co-incubated with 1 μ M TO-PRO-3 iodide (Invitrogen, T3605). Embryos were cleared in 70% glycerol. Labeled cells were counted manually, one eye per embryo (ImageJ, NIH).

Imaging

Embryos (12 hpf) were dechorionated, embedded in 1.5% low-melting-point agarose (in E2 plus gentamycin) in DeltaT dishes (Bioptechs, #0420041500C). Images were acquired using an Olympus FV1000 laser-scanning confocal microscope. Plates were overlaid with E2 plus gentamycin and covered to prevent evaporation. No stage heater was used; the room was 27.6 \pm 0.4°C and the stage slightly warmer. Based on when the lens pinches off (24 hpf), we estimate that sample temperature was very close to 28.5°C. Four-dimensional datasets were acquired: 38 z-sections, 3.52 μ m z-step, 3.15 minutes between z-stacks, 40 \times water-immersion objective (1.15 NA).

Kaede photoconversion used Olympus FluoView software to expose a region of interest (R.O.I.) to 405 nm light for 15–20 seconds. Efficiency was assayed by photoconversion of green to red fluorescence in the R.O.I.

Image processing and analysis

Before cell tracking, 4D datasets were processed: files were converted to multilayer single time point TIFFs; using the Float Morphology plug-in (ImageJ), the 'open' function was applied for the nuclear channel and the 'close' function for the membrane channel; the membrane channel was subtracted from the nuclear channel to improve nuclear separation; finally, intensity was adjusted along the z-axis to compensate for dimmer signals in deeper, ventral tissue.

Images were processed using ImageJ and Adobe Photoshop. Volume rendering was performed using Amira (Visage Imaging) or FluoRender (Wan et al., 2009). Three-dimensional cell speed was quantitated using Excel (Microsoft). Quantitative data were analyzed using analysis of variance (ANOVA) and *P*-values determined using Tukey's HSD test.

LongTracker

For cell tracking, we used the MATLAB-based program LongTracker to select nuclei at specific time points and z positions, while simultaneously viewing xz and yz reslices and adjacent frames in z and t, stepping through the dataset forward or backward in time. For accurate cell tracking, we required at least 50% nuclear pixel overlap between time points. Data were exported as a spreadsheet of nuclear centroid position and nuclear TIFF images. Trajectories were checked for discontinuities in four dimensions using FluoRender.

Volume measurements and cell counting

Tissue volumes were measured using Amira after manual segmentation based on the membrane channel. Using the same manual segmentation, cell number was quantitated using the nuclear channel and the program EVE (T. Shimada, University of Tokyo), after applying an interpolation step to decrease the anisotropy of the data. Between each pair of adjacent slices a new slice – the average of the pair – was inserted.

Visualization and quantitation of mitoses

Mitoses were marked using LongTracker. Classification as a mitosis required unambiguous identification of a metaphase plate and two subsequent daughter nuclei. LongTracker allowed us to identify mitoses that spanned multiple z-slices while avoiding double counting. Mitosis tracking data were visualized in four dimensions (FluoRender) and quantitated (Excel).

Chick fate mapping

Fertilized White Leghorn chicken eggs were incubated at 38°C until the appropriate stage (Hamburger and Hamilton, 1992). Embryos were removed from eggs using filter paper rings and cultured, ventral side up, in dishes filled with agarose-albumen medium (0.2% agarose, 50% albumen) at 37°C, 10% CO₂ (EC culture) (Chapman et al., 2001). For DiI injection, embryos were flipped dorsal side up, and access to the OV attained via a small incision in the vitelline membrane. DiI (Molecular Probes, D282; 0.25% in 1:20 DMSO:tetracycline) or CM-DiI (Molecular

Probes, C7000; 0.125% in 1:2 DMSO:tetraglycol) was applied; embryos were immediately imaged and returned to culture. Embryos were fixed with 4% PFA in PBS, counterstained with DAPI or Hoechst 33342, stepped through a glycerol/PBT (PBS containing 0.1% Triton X-100) gradient to a final concentration of 80% glycerol in double-distilled H₂O, and reimaged. Imaging was performed with a Leica SP5 laser-scanning confocal microscope. Volume rendering and image analysis were performed using FluorRender.

RESULTS

Time-lapse imaging of eye morphogenesis

To visualize directly the cellular basis of OCM, we generated 4D datasets using time-lapsed fluorescence confocal microscopy. Embryos were labeled for membranes (EGFP-CAAX) and nuclei (H2A.F/Z-mCherry) by RNA injection at the one-cell stage and imaged 12–24 hours post-fertilization (hpf; supplementary material Movie 1; see Materials and methods). Since our datasets show little bleaching and no bright pyknotic nuclei indicative of phototoxicity, we believe that our imaging does not perturb OCM, except for a slight flattening (on the dorsal side) caused by mounting.

Single confocal images (Fig. 1B–F) from a representative dataset show membrane and nuclear labeling; volume renderings (Fig. 1B'–F', B''–F'') illustrate changes in tissue shape and size. By 12 hpf (Fig. 1B–B''), the OV (purple) is a flat, wing-like structure emerging from the neural keel. By 14 hpf (Fig. 1C–C''), it has elongated posteriorly, assuming a flipper-like shape, and a furrow (Fig. 1A, arrowhead) drives anteriorly to constrict the connection between eye and brain, generating the presumptive optic stalk. OV invagination commences at 16 hpf (Fig. 1D–D''); the overlying ectoderm thickens, forming the lens placode (yellow). The lens is essentially round at 20 hpf (Fig. 1E–E''), as the OV envelops it. Finally, at 24 hpf (Fig. 1F–F''), the lens has pinched off from the ectoderm and OCM is complete.

The optic vesicle increases in both volume and cell number during morphogenesis

As a first step toward determining underlying cellular mechanisms, we measured OV volume and cell number in 4D datasets. Its volume increased only moderately (46%) over 12 hours (from $0.84 \pm 0.06 \times 10^6$ to $1.23 \pm 0.12 \times 10^6 \mu\text{m}^3$, mean \pm s.d.; $n=3$), with most of the increase between 12 and 16 hpf (Fig. 2A, supplementary material Fig. S1B). In previous measurements of fixed samples (Li et al., 2000), OV volumes were ~40% smaller due to fixation, but there was little change between 16 and 24 hpf, in agreement with our data.

Distinct lateral (ll) and medial (ml) OV layers are first distinguishable at 16 hpf (Fig. 1D). The lateral layer is often considered presumptive NR and the medial layer presumptive RPE (but see below). At 16 hpf, the layers were similar in size (ll, $0.65 \pm 0.11 \times 10^6 \mu\text{m}^3$; ml, $0.52 \pm 0.08 \times 10^6 \mu\text{m}^3$; Fig. 2A, supplementary material Fig. S1B). From 16–24 hpf (during invagination), this changes dramatically: the lateral layer expands to greater than four times the volume of the thinning medial layer (ll, $1.00 \pm 0.10 \times 10^6 \mu\text{m}^3$; ml, $0.23 \pm 0.02 \times 10^6 \mu\text{m}^3$; Fig. 2A, supplementary material Fig. S1A). The lens is first visible at ~15 hpf as a slight thickening of the overlying ectoderm. It grows steadily until ~23 hpf, then pinches off from the ectoderm, comprising ~10% of the OC volume ($0.13 \pm 0.02 \times 10^6 \mu\text{m}^3$; Fig. 2A, supplementary material Fig. S1A,B). Changes in relative volumes were highly reproducible (Fig. 2A, supplementary material Fig. S1A,B).

During OCM, cell number roughly doubled, from 1142 ± 78 (12 hpf) to 2467 ± 76 (24 hpf) (Fig. 2B, supplementary material Fig. S1C), with half of the increase occurring from 12–16 hpf (1142 ± 78 to 1805 ± 222), before invagination. Relative cell numbers were very consistent between embryos (supplementary material Fig. S1C). Cell density increased gradually (supplementary material Fig. S1D).

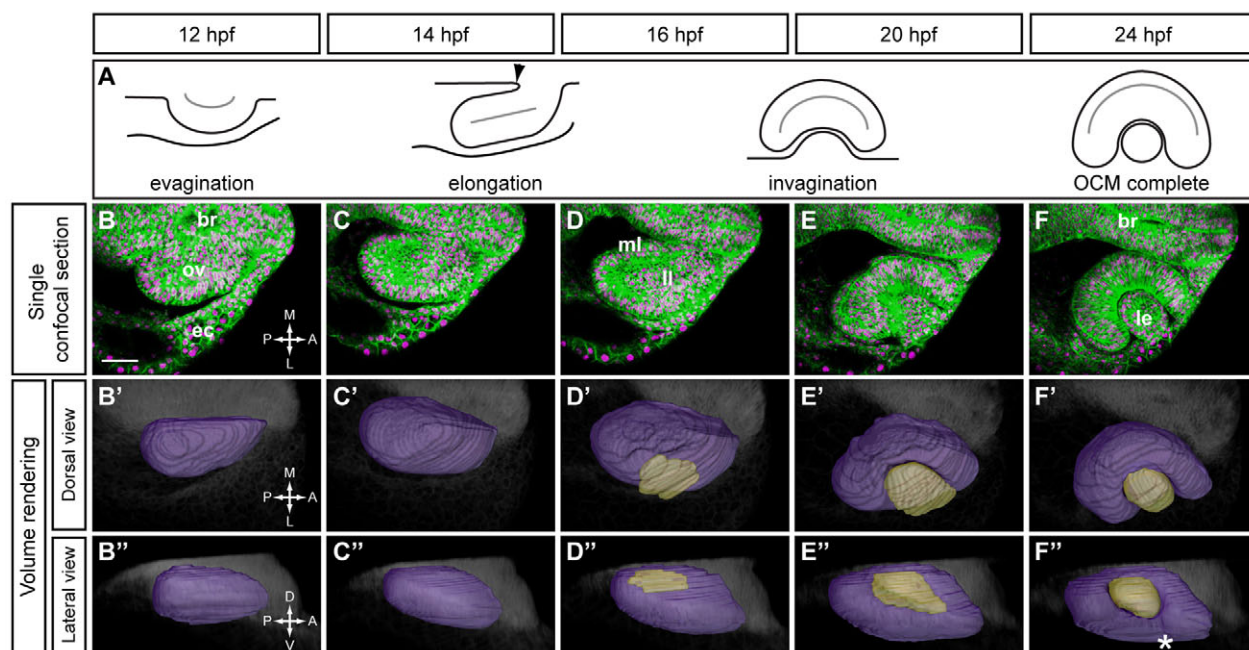


Fig. 1. Timecourse of optic cup morphogenesis in zebrafish. (A) Schematic of optic cup morphogenesis (OCM), dorsal view. Arrowhead, furrow constricting the optic stalk. (B–F) Single confocal slices from 4D dataset of right optic vesicle (OV) at 12–24 hpf showing EGFP-CAAX (membranes, green) and H2A.F/Z-mCherry (nuclei, magenta). Dorsal views. (B'–F', B''–F'') Volume renderings. OV (purple), lens (beige), brain (gray). (B'–F') Dorsal views. (B''–F'') Lateral views. Asterisk, choroid fissure. br, brain; ov, optic vesicle; ec, ectoderm; ml, medial layer; ll, lateral layer; le, lens; A, anterior; P, posterior; M, medial; L, lateral; D, dorsal; V, ventral. Scale bar: 50 μm .

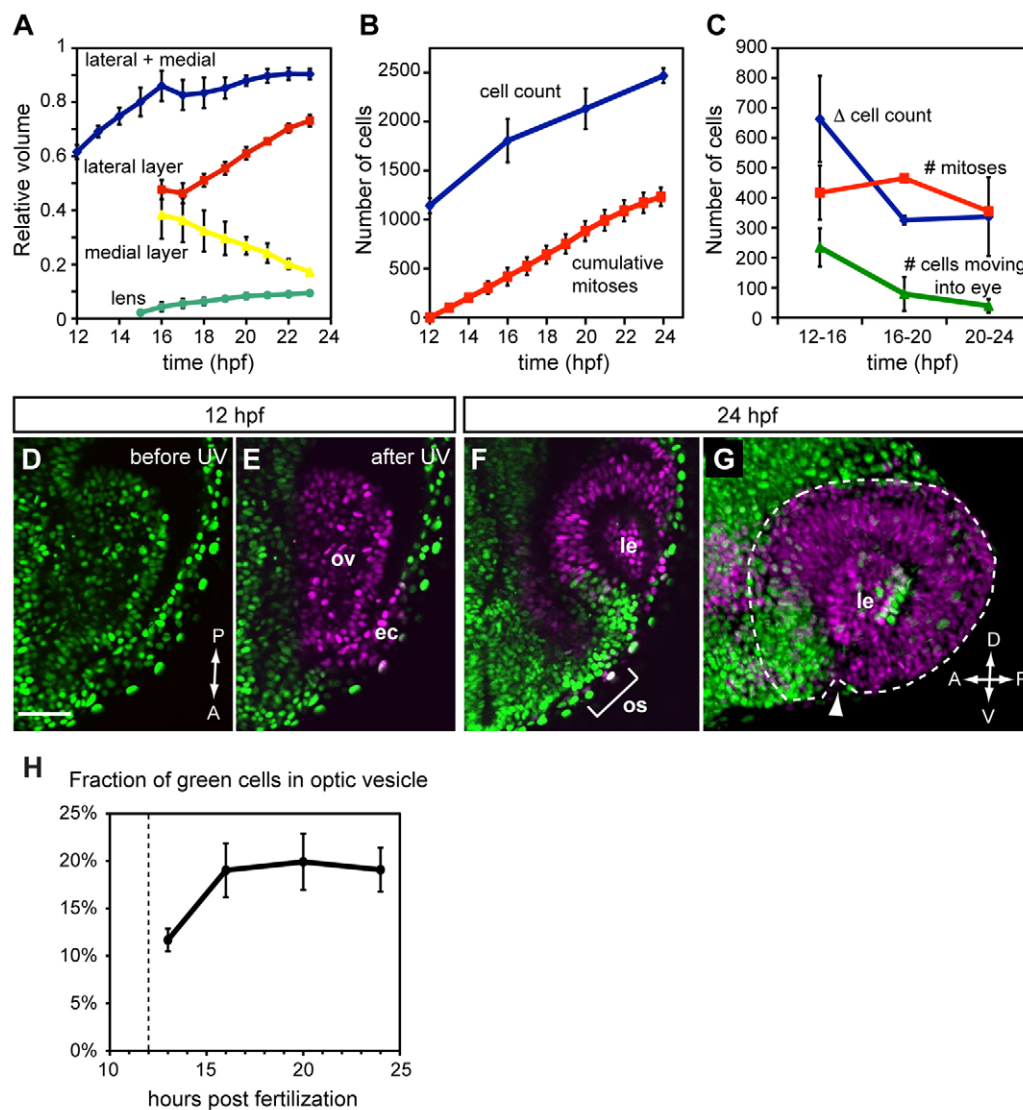


Fig. 2. Quantitative analysis of growth, proliferation and extended evagination during OCM.

(A) Relative volume of OV (blue), OV lateral layer (red), OV medial layer (yellow) and lens (green) as a fraction of final volume (OV plus lens). $n=3$.

(B) Cell count (blue) and mitoses (red). $n=2$. (C) Cell count change (blue), mitoses (red) and number of cells moving into eye (green). $n=2$ for cell count and mitoses; $n=3$ for evagination.

(D) Single confocal section (dorsal view) of OV at 12 hpf showing nls-Kaede (green) before photoactivation.

(E) After photoactivation, the entire OV (and some ectoderm) is converted to red (magenta).

(F) Single confocal section (dorsal view) of the same embryo at 24 hpf showing green nuclei in the anterior OC and optic stalk.

(G) A 3D-rendered lateral view of same OC. Arrowhead, choroid fissure. The optic cup is outlined.

(H) Quantification of extended evagination showing the fraction of green cells within the OV ($n=3$). Dashed line indicates the time of photoactivation (12 hpf). Only OV cells, not overlying lens/ectoderm, were counted. ec, ectoderm; ov, optic vesicle; os, optic stalk; le, lens. Error bars indicate s.d. Scale bar: 50 μ m.

Can proliferation alone account for this increase in cell number? Mitoses are easily recognizable in our 4D datasets; H2A.F/Z-mCherry marks the elongated metaphase plate. We manually counted all mitoses (supplementary material Fig. S1E,F; see Materials and methods) and did not observe any obvious patterns of mitosis in our datasets (supplementary material Movie 2). The number of dividing cells was constant throughout OCM, with a slight plateau after ~ 21 hpf (Fig. 2B). Comparing changes in cell number with the number of mitoses shows that proliferation does not account for the rapid increase in cell number from 12–16 hpf (417 ± 90 mitoses versus 663 ± 144 additional cells; Fig. 2B,C). This suggests that, surprisingly, cells continue to enter the OV after 12 hpf, when evagination is thought to be complete.

We therefore directly counted cells moving from brain to eye after 12 hpf, using a nuclear-localized (nls) version of the fluorophore Kaede (Fig. 2D–H), which is converted from green to red fluorescence by irreversible photocleavage (Ando et al., 2002). At 12 hpf, the entire OV was photoconverted (Fig. 2D,E). Thus, any green nuclei in the eye thereafter (omitting overlying ectoderm/lens) must have entered from the brain during extended evagination. The 235 ± 64 cells moving from brain to OV between 12 and 16 hpf neatly account for the difference between the

increase in cell count (663 ± 144) and mitotic count (417 ± 90) (Fig. 2C). Late evagination ends by 16 hpf; the fraction of green nuclei thereafter remained roughly constant ($\sim 19.1\%$; Fig. 2H). Interestingly, late-moving cells specifically populated the ventroanterior OC (Fig. 2F,G). A similar extended evagination, in which late-moving cells populate the ventral OC, was reported in *Xenopus*, although without a detailed timecourse (Holt, 1980). Thus, this phenomenon might be a conserved feature of vertebrate OCM.

After 16 hpf, the number of mitoses matched or exceeded the change in cell number (Fig. 2C), implying that cell division and death can completely account for changes in cell number. However, although these quantitative analyses reveal the role of proliferation in controlling cell number, they do not address its role in morphogenesis.

Mitosis is dispensable for basic aspects of OCM

Inhibiting proliferation does not affect retinal cell type differentiation in *Xenopus*; however, the resulting eyes are small and disorganized (Harris and Hartenstein, 1991). OCM completion, however, was not analyzed as a time point and it is a formal possibility that loss of mitosis specifically during OCM could have

caused disorganization. In addition, this has not been tested in zebrafish. To test the role of proliferation specifically during zebrafish OCM, we incubated embryos in the DNA synthesis inhibitors hydroxyurea and aphidicolin (HUA) from 10.5–24 hpf, then analyzed effects on OCM. HUA treatment, as assayed by phospho-histone H3 staining (Fig. 3D–F), inhibited mitosis by ~87% (untreated, 74 ± 16 mitoses per eye; DMSO, 62 ± 13 ; HUA treated, 8.3 ± 3.8 ; Fig. 3G).

HUA-treated OV's contained significantly fewer cells (826 ± 121) than untreated (2235 ± 296) or DMSO-treated (1895 ± 295) OV's (Fig. 3H). OV volume decreased modestly from $1.15 \pm 0.11 \times 10^6 \mu\text{m}^3$ (untreated) or $0.99 \pm 0.07 \times 10^6 \mu\text{m}^3$ (DMSO) to $0.84 \pm 0.12 \times 10^6 \mu\text{m}^3$ (HUA treated; Fig. 3I). HUA-treated cells were distinctly larger (Fig. 3B,C), as reflected in a roughly halved cell density [1.0 ± 0.1 (HUA) versus 1.9 ± 0.3 (DMSO) or 1.9 ± 0.1 (untreated) nuclei/ $10^3 \mu\text{m}^3$].

Despite effects on cell number and size, morphogenesis proceeded normally (Fig. 3A–C). HUA-treated eyes were smaller but not disorganized, containing recognizable NR, RPE and lens (Fig. 3C), suggesting that the previously observed disorganization arose during retinal neurogenesis. The retina enwrapped the lens slightly less than normal, but this might be due to decreased retina and RPE cell number. The fraction of OC volume occupied by RPE was similar to that of controls (untreated, 0.21 ± 0.02 ; DMSO treated, 0.21 ± 0.05 ; HUA treated, 0.24 ± 0.02 ; Fig. 3K), indicating that the RPE thins and the NR thickens normally. Therefore, although mitosis contributes to changes in cell number, organ volume and cell density, it is dispensable for the basic program of OCM.

Tracking cell movements during OCM

Setting mitosis aside, we hypothesized that OCM relies primarily on cell movements. Therefore, we tracked cell movements in four dimensions, mapping the discrete morphogenetic events underlying OCM. We developed a MATLAB-based program, LongTracker, for manual cell tracking (H.O., K.R.C., Y. Wan, K.M.K., C. Hansen, C. K. Rodesch and C.-B.C., unpublished; see Materials and methods). Accurate cell tracking allows us to analyze cell movements and interrogate 4D datasets for cell fates, either prospectively or retrospectively. Importantly, many cells can be tracked from a single dataset, obviating the need to superimpose positional information from many embryos (a necessarily noisy process).

Although laborious, manual cell tracking was successful. In total, we tracked 153 cells from three datasets, with most tracking from the primary dataset and the two others used for confirmation (supplementary material Table S1). In the primary dataset, ~3% of OC cells were tracked from retina, RPE and lens. All data shown in the following figures are derived from the primary dataset. Combining our cell tracking with ImageJ, Amira and FluoRender for visualization, we defined the component cell movements of OCM and the timeline of movements, and generated a fate map of eye subdomains based on cell position and trajectory.

Retinal cell movements

We defined four major prospective NR movements: extended evagination, elongation (pinwheel movement), rim movement and anterior rotation.

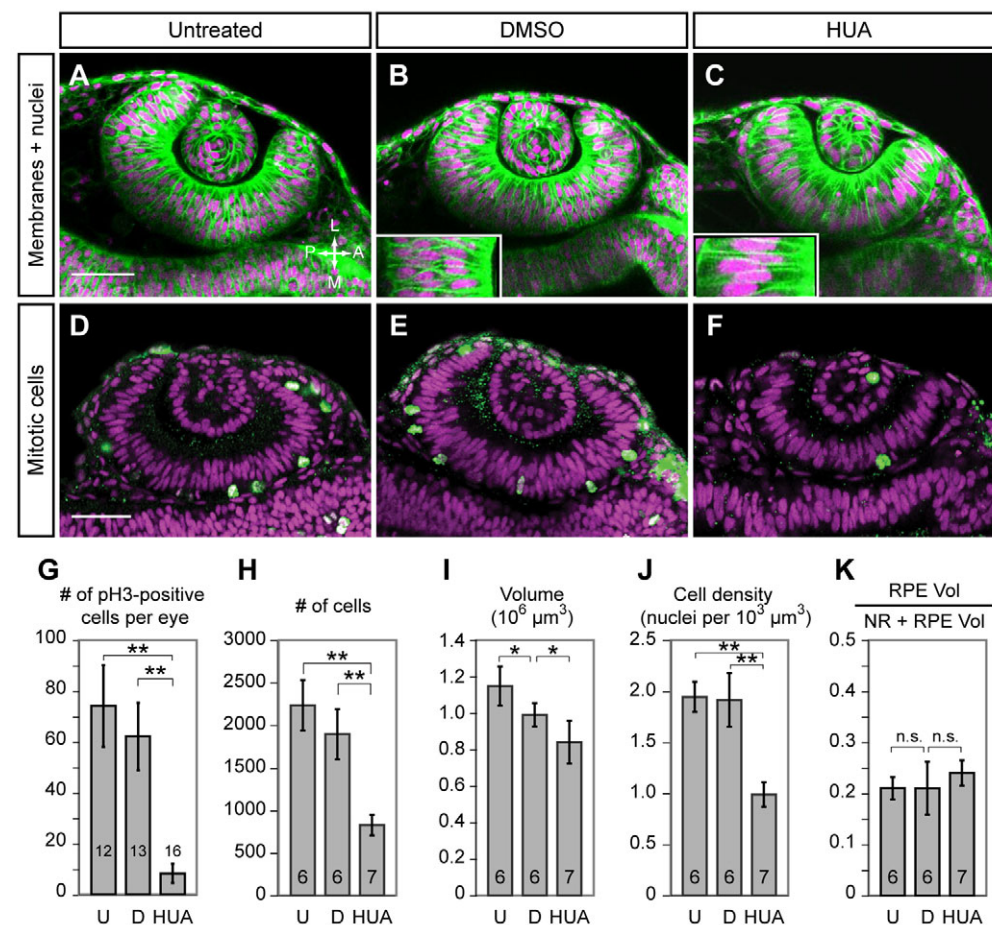


Fig. 3. Proliferation is dispensable for OCM.

(A–C) Confocal sections (live, 24-hpf) showing EGFP-CAAX (membranes, green) and H2A.F/Z-mCherry (nuclei, magenta). (A) Untreated, (B) DMSO and (C) HUA embryos treated from 10.5–24 hpf. Insets show large HUA-treated cells versus DMSO control. (D–F) Confocal sections at 24 hpf showing phospho-histone H3 (green) and TO-PRO-3 (magenta) in (D) untreated, (E) DMSO-treated and (F) HUA-treated embryos. Dorsal view. (G–K) Quantitative analyses of (G) mitoses, (H) cell number, (I) OV volume, (J) cell density and (K) retinal pigmented epithelium (RPE) volume as a fraction of OC [neural retina (NR) plus RPE] at 24 hpf in untreated (U), DMSO-treated (D) and HUA-treated embryos. Numbers of embryos scored (one eye each) are indicated within each bar. *, $P < 0.05$; **, $P < 0.01$; error bars indicate s.d. Scale bars: 50 μm .

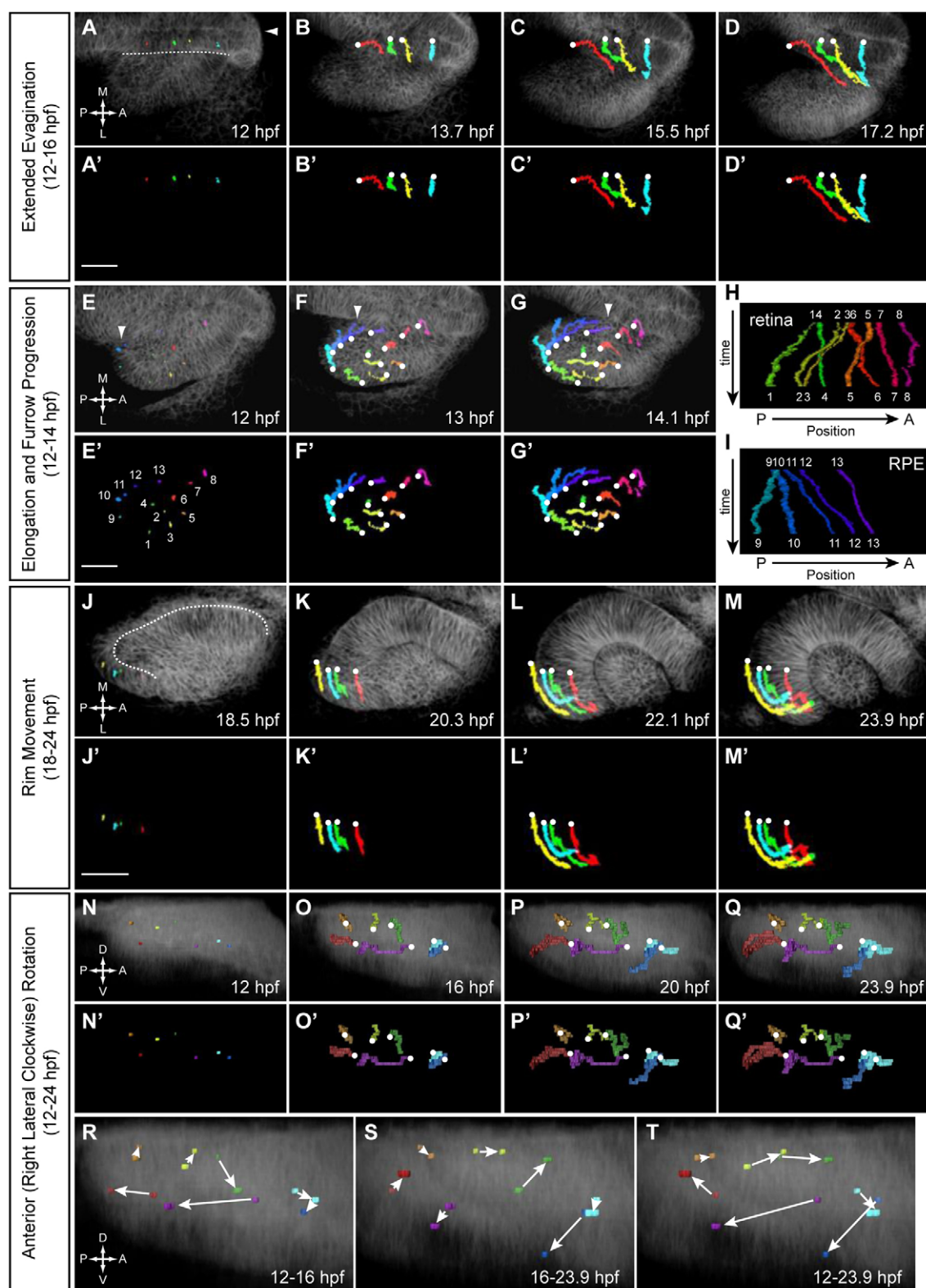


Fig. 4. Four major retinal cell movements during OCM. (A-D') Extended evagination (12-16 hpf). Cells are moving from brain to eye. Arrowhead, embryo midline; dotted line, OV/brain boundary. (A-D) Trajectories over membrane channel average projection (grayscale). (A'-D') Trajectories only. (E-G') OV elongation (12-14 hpf). Thirteen cells (1-8 NR, 9-13 RPE) undergoing pinwheel movement. Arrowhead, leading edge of furrow. (E-G) Trajectories over membrane channel average (grayscale). (E'-G') Trajectories only. (H,I) Kymographs showing change in AP position over time for NR (H) and RPE (I) cells. (J-M') Rim movement (18-24 hpf). Cells are moving from the medial to lateral layer. (J-M) Trajectories over membrane channel average (grayscale). (J'-M') Trajectories only. Dotted line (J) demarcates the medial and lateral layers. (N-Q') Eye rotation (12-24 hpf). (N-Q) Trajectories over volume rendering of membrane channel (grayscale). (N'-Q') Trajectories only. (R-T) Rotation summaries for (R) 12-16 hpf, (S) 16-23.9 hpf and (T) 12-23.9 hpf. White circles indicate origins. (A-G',J-M') Dorsal view. (N-T) Lateral view. Scale bars: 50 μ m.

Extended evagination (12-16 hpf)

Zebrafish OV evagination had been thought complete by 12 hpf (Schmitt and Dowling, 1994). Quantitative analysis shows that although most evagination is complete by 12 hpf, it continues for ~4 hours (Fig. 2D-H). Cell tracking also clearly demonstrates this (Fig. 4A-D', supplementary material Movie 3). Four representative cells crossed from brain into OV, clearly occupying the OV by 17.2 hpf (Fig. 4C,D).

OV elongation: pinwheel movement (12-14 hpf)

OV elongation has been described in several vertebrates using fixed tissue analysis, but not its underlying mechanism (Hilfer, 1983; Schmitt and Dowling, 1994; Schook, 1980b; Silver, 1981). In zebrafish, the OV rapidly shifts from wing-like to a posteriorly elongated flipper-like shape (Fig. 1). In chick, localized proliferation was proposed to underlie OV elongation (Hilfer et al., 1981). We find only a slight posterior bias for mitosis during this period (58.7% of mitoses occur in the posterior OV; $n=2$). Instead, prospective NR and RPE cells (definitively identified by backtracking) participate in a rapid, coordinated pinwheel movement (Fig. 4E-G', supplementary material Movie 4). Prospective NR streamed into the OV, moving posteriorly (tracked cells 1-3, 5) and laterally (cells 6-8) (Fig. 4H), while prospective RPE (cells 9-13) moved medially and anteriorly (Fig. 4I). Considering all tracked cells (not just the representatives shown), more cells moved posteriorly than anteriorly, resulting in net posterior growth. Underscoring the rapidity of this movement, prospective NR moved faster during elongation than during the following 2 hours (1.03 ± 0.26 versus 0.84 ± 0.14 $\mu\text{m}/\text{minute}$, mean \pm s.d.; supplementary material Fig. S2).

Rim movement (18-24 hpf)

The OV medial layer shrinks dramatically starting at 16 hpf, with concomitant growth of the lateral layer (Fig. 2A, supplementary material Fig. S1B). A previous 3D time-lapse study showed migration from the medial to lateral layer around the ventral rim, at the AP level of the optic stalk (Picker et al., 2009). We found such movements throughout the OV.

During invagination (18-24 hpf), medial layer cells involuted around the rim, joining the lateral layer, on both anterior and posterior margins of the OV (posterior shown, Fig. 4J-M', supplementary material Movie 5). We saw no evidence of cells ingressing directly across the optic lumen, confirming a previous hypothesis (Li et al., 2000). Our data reveal the temporal extent of this movement (18-24 hpf) and, taken together with the ventral rim movement previously observed (Picker et al., 2009), show that rim movement occurs around most (if not all) of the OV circumference, providing an explanation for the reciprocal volume changes of the two layers.

Anterior rotation (12-24 hpf)

Based on fixed tissue analysis, it was proposed that the eye rotates during the two stages of cephalic flexure [14-15 hpf and 24-36 hpf (Schmitt and Dowling, 1994)], bringing the choroid fissure to its final ventral position. This rotation is clockwise in a right lateral view (counterclockwise in a left lateral view), distinct from the pinwheel movement described above and viewed in a perpendicular plane. At 24 hpf, the choroid fissure lies 20-30° anterior of the ventral pole of the eye (Fig. 1F'', asterisk).

Cell tracking revealed some rotation during the first stage of cephalic flexure (Fig. 4N-O', R). However, this rotation continued over the next 8 hours, before the second stage (Fig. 4O-Q', S), with

all cells moving clockwise during OCM to different extents (Fig. 4T). Thus, eye rotation might not be a passive result of cephalic flexure, but an active independent motion. Alternately, cephalic flexure might not be restricted to distinct stages, but a continuous gradual movement.

Origin of retinal domains

Since we tracked cells throughout the NR and found little cell mixing, we could draw the first complete retina fate map. We clustered all tracked NR cells from the primary dataset (Fig. 5A,D, supplementary material Fig. S3A-F, Movie 6, Table S2) into dorsal, ventral, anterior, central and posterior domains, based on final 24-hpf position and trajectory shape (Fig. 5B,C,E,F, supplementary material Movie 7). Because not all cells were tracked, domain boundaries are somewhat imprecise. Within each domain, all cells traveled along similar trajectories (Fig. 5G-L, supplementary material Movie 8), except for ventral.

In a lateral view of the 12-hpf OV (Fig. 5C), the dorsal, anterior, ventral and posterior domains are arranged circumferentially, behind the laterally situated central domain. As OCM proceeds, the peripheral domains rotate circumferentially (clockwise, right lateral view), while the central domain inserts into the hub of the wheel (Fig. 5F). This model confirms and extends a previous anterior retina fate map (Picker et al., 2009).

A surprise was the central domain, which we separated out only after noting the unique, 'gamma-shaped' trajectories of the cells (Fig. 5I). Cells moved posteriorly during OV elongation, then executed a loop turn and moved medially during invagination. How does the central domain merge into the OC center? It might actively push into position, or instead might be passively encircled by other domains. To test both models, we tracked anterior, central and posterior cells (Fig. 5Q-U', supplementary material Movie 9). From 14-18 hpf (Fig. 5R-S'), after elongation, central cells (blue) have not moved significantly, while posterior (yellow) and anterior (orange) cells have bypassed them on either side, effectively completing the merge. Subsequently, central cells finally begin to move medially as invagination ends (20-24 hpf; Fig. 5T-U'). We conclude that the central domain merges into the OC hub in a largely passive manner, while cells in other domains migrate around the central domain, encircling it.

To confirm these results independently, we performed Kaede fate mapping: small clusters of cells were marked and imaged at 12 hpf (Fig. 5M,O) and 24 hpf (Fig. 5N,P). Clusters stayed relatively compact, with occasional extraocular labeling due to photoconversion of overlying or underlying cells. We present two typical examples. Lateral OV cells approximately halfway along the AP axis at 12 hpf (Fig. 5M) resided in the central retina at 24 hpf (Fig. 5N), confirming central domain tracking. Medial OV cells (adjacent to the brain) approximately one-third from its anterior end at 12 hpf (Fig. 5O) resided in the anterior retina by 24 hpf (Fig. 5P). Extensive Kaede experiments ($n=40$) confirmed the NR fate map based on cell tracking.

RPE cell movements

Tracking revealed two major RPE movements: pinwheel movement and spreading.

OV elongation: pinwheel movement (12-14 hpf)

During OV elongation and anterior furrow progression, prospective RPE cells participated in the pinwheel movement described above. The representative RPE cells shown (tracked cells 9-13) moved in a single, coordinated pinwheel trajectory with NR (Fig. 4E-G',

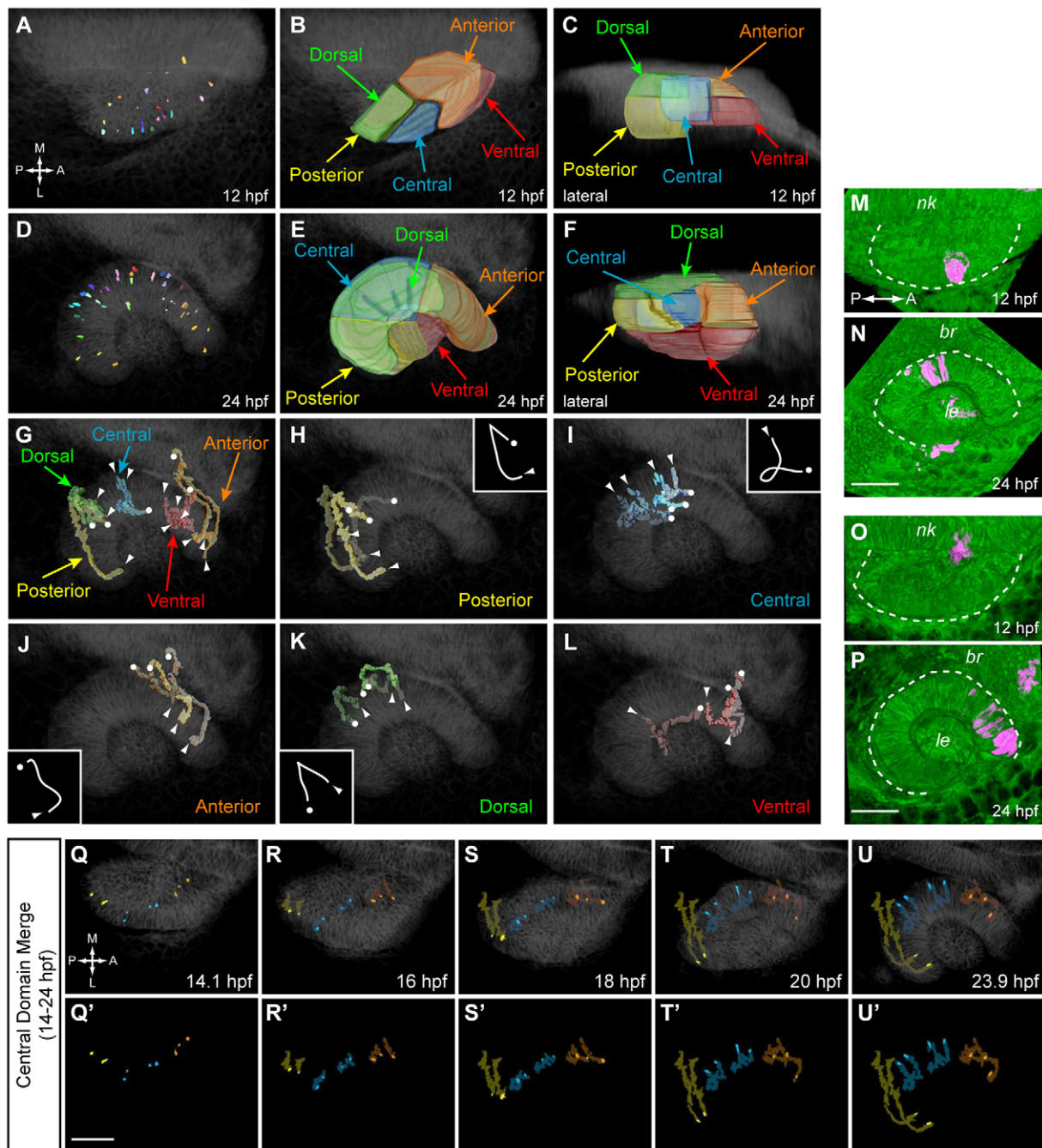


Fig. 5. Origin and movement of retinal subdomains. (A,D) Positions of tracked NR cells at 12 (A) and 24 (D) hpf. Dorsal views. (B,C) Volume rendering of retinal subdomains (12 hpf): posterior (yellow), central (blue), anterior (orange), dorsal (green) and ventral (red). (B) Dorsal view. (C) Lateral view. (E,F) Volume rendering of retinal subdomains (24 hpf). (E) Dorsal view. (F) Lateral view. (G-L) Retinal subdomain trajectories. Dorsal view. Circles indicate origins; arrowheads indicate termini. (G) Summary. (H-L) Individual subdomains. Insets illustrate typical trajectory shape, except for ventral, which has none. (M-P) Kaede fate mapping. Dorsal views, volume renderings. (M,O) OV at 12 hpf; photoactivated spot, magenta. (N,P) Final position after OCM (24 hpf). (M,N) Central domain. (O,P) Anterior domain. Dashed lines outline OV (12 hpf) and OC (24 hpf). (Q-U') Central domain merge (14-24 hpf): posterior (yellow), central (blue) and anterior (orange) trajectories. Dorsal views. (Q-U) Trajectories over membrane channel average (grayscale). (Q'-U') Trajectories alone. nk, neural keel; br, brain; le, lens. Scale bars: 50 μm.

supplementary material Movie 4) medially and either slightly posteriorly (cell 9) or anteriorly with the furrow (cells 10-13; Fig. 4I). Again, cells moved rapidly, with a mean 3D speed of 1.17 ± 0.17 μm/minute during elongation, slowing to 0.84 ± 0.10 μm/minute in the subsequent 2 hours (supplementary material Fig. S2).

Spreading (14-24 hpf)

After pinwheel movement, the prospective RPE spreads dramatically to become a flat monolayer: the distance between nuclei increases greatly, and cells spread to cover the back of the NR (Fig. 6A-D', supplementary material Movie 10).

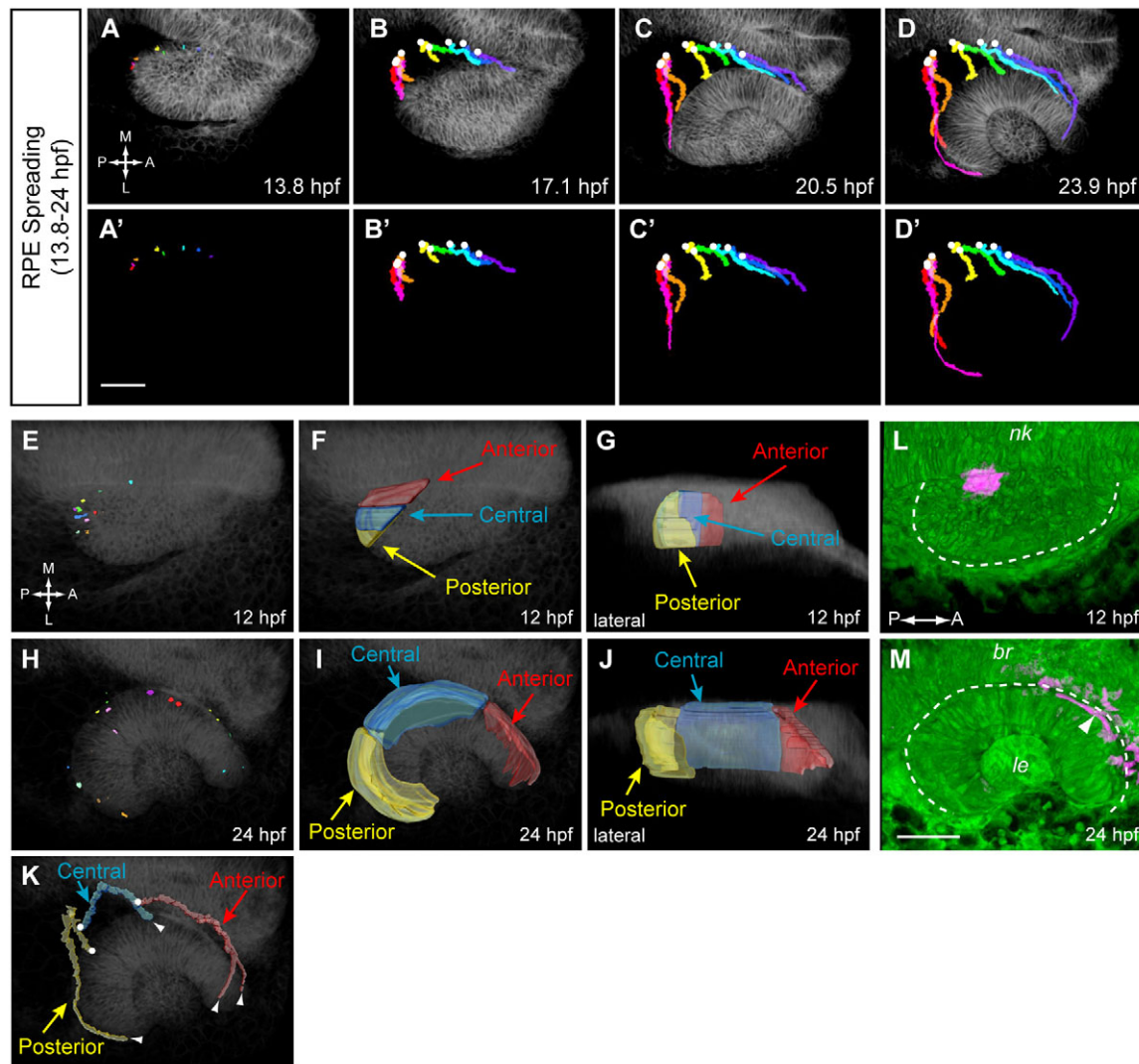


Fig. 6. RPE cell movements and origin of RPE subdomains. (A-D') RPE spreading (13.8-24 hpf). Dorsal view. (A-D) Trajectories over membrane channel average (grayscale). (A'-D') Trajectories alone. Circles indicate origins. (E,H) Positions of tracked RPE cells at 12 (E) and 24 (H) hpf. Dorsal view. (F,G) Volume rendering of RPE subdomains (12 hpf); posterior (yellow), central (blue), anterior (red). (F) Dorsal view. (G) Lateral view. (I,J) Volume rendering of RPE subdomains (24 hpf). (I) Dorsal view. (J) Lateral view. (K) RPE subdomain trajectories (dorsal view). Circles indicate origins; arrowheads indicate termini. (L,M) Kaede fate mapping. Dorsal views. Volume renderings. (L) OV (12 hpf); photoactivated spot, magenta. (M) Final position after OCM (24 hpf) as indicated by arrowhead. Dashed line outlines OV (12 hpf) and OC (24 hpf). nk, neural keel; br, brain; le, lens. Scale bars: 50 μ m.

Origin of RPE domains

We generated an RPE subdomain fate map by clustering all tracked RPE cells in the primary dataset (Fig. 6E,H, supplementary material Fig. S3G-J, Movie 11, Table S2) into three domains – anterior, central and posterior – based on final 24-hpf position and trajectory shape (Fig. 6F,G,I,J, supplementary material Movie 12). Within each domain, cells traveled along similar trajectories (Fig. 6K, supplementary material Movie 8). Our fate map omitted the ventral eye, where diminished image quality precluded reliable tracking.

The posterior RPE domain initially abutted the posterior and dorsal retinal domains, whereas the anterior RPE initially abutted anterior and ventral retina. Interestingly, we find similar trajectories for neighboring RPE and retina cells. For example, posterior retina (Fig. 5G,H) and posterior RPE (Fig. 6K) both travel along a similar hook-shaped trajectory (supplementary material Movie 8). Therefore, neighboring tissues move in concert, regardless of eventual cell fate.

Again, we confirmed our manual tracking using Kaede fate mapping ($n=7$). A photoactivated spot within the anterior RPE domain at 12 hpf (Fig. 6L) gave rise to anterior RPE cells at 24 hpf (Fig. 6M, arrowhead) and some brain cells.

Lens cell movements

We observed two prospective lens movements: pinwheel movement and compaction.

OV elongation: pinwheel movement (12-14 hpf)

During OV elongation, surprisingly, prospective lens cells followed the same trajectory as underlying retinal cells (Fig. 7A-D, supplementary material Movie 13). Again, cells moved rapidly during elongation, with a mean 3D speed of $1.01 \pm 0.27 \mu\text{m}/\text{minute}$, slowing to $0.80 \pm 0.12 \mu\text{m}/\text{minute}$ in the subsequent 2 hours (supplementary material Fig. S2). These speeds are strikingly similar to those of

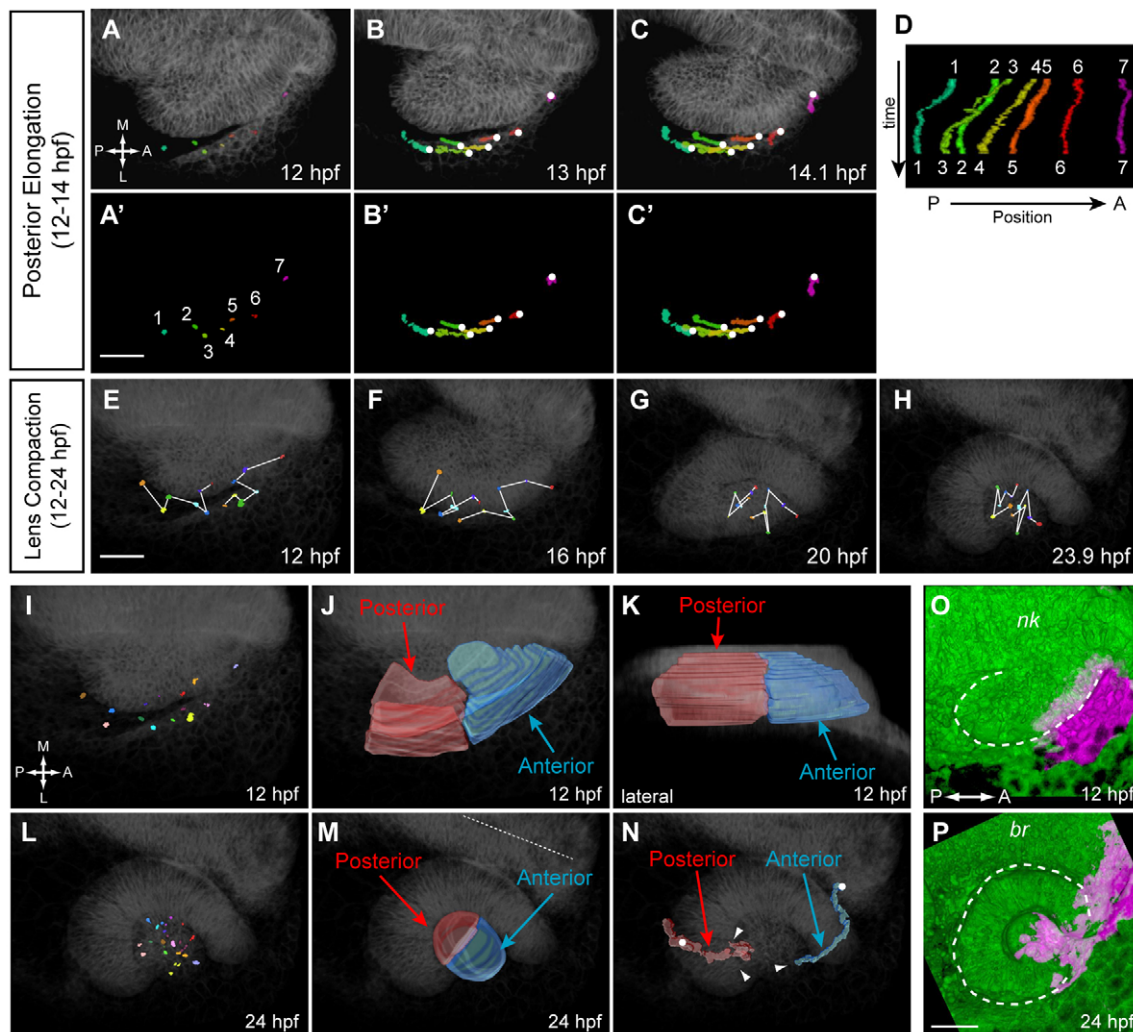


Fig. 7. Lens cell movements and origin of lens domains. (A-C') OV elongation (12-14 hpf). Dorsal views. (A-C) Trajectories over membrane channel average (grayscale). (A'-C') Trajectories alone. Circles indicate origins. (D) Kymograph showing change in cell AP position over time. (E-H) Lens compaction and cell mixing (12-24 hpf). Dorsal views. (I, L) Positions of tracked lens cells at 12 (I) and 24 (L) hpf. Dorsal views. (J, K) Volume rendering of lens subdomains (12 hpf); posterior (red), anterior (blue). (J) Dorsal view. (K) Lateral view. (M) Volume rendering of lens subdomains (24 hpf). Dorsal view. Dotted line indicates midline. (N) Lens subdomain trajectories (dorsal view). Circles indicate origins; arrowheads indicate termini. (O, P) Kaede fate mapping. Dorsal views. Volume renderings. (O) OV (12 hpf); photoactivated region, magenta. (P) Final position after OCM (24 hpf). Dashed line outlines OV (12 hpf) and OC (24 hpf). nk, neural keel; br, brain. Scale bars: 50 μ m.

prospective retinal cells ($1.03 \pm 0.26 \mu\text{m}/\text{minute}$ during elongation, slowing to $0.84 \pm 0.14 \mu\text{m}/\text{minute}$). Therefore, although lens cells do not appear to directly contact the OV their movement appears coordinated, with the same direction and speed as underlying NR.

Compaction (12-24 hpf)

Prospective lens cells originate throughout the entire ectoderm overlying the OV. During lens formation, they compact dramatically. Skeletons were drawn linking seven anterior and seven posterior cells (Fig. 7E-H). From 12-24 hpf, the skeletons collapsed. Interestingly, although cells appeared to mix, the skeletons remained separated (see below).

Origin of lens domains

We generated a lens subdomain fate map. All tracked lens cells from the primary dataset (Fig. 7I, L, supplementary material Fig. S3K-L, Movie 14, Table S2) were clustered according to final 24-hpf position

and trajectory shape. As noted above, we found more mixing among lens cells than among NR or RPE (Fig. 7E-H). Only one boundary was evident in this dataset, dividing anterior (superficial) from posterior (deep) lens halves at 24 hpf (Fig. 7M, supplementary material Movie 15). This boundary corresponded to a border dividing the AP axis of the ectoderm at 12 hpf (Fig. 7J, K, supplementary material Movie 15). The two skeletons (Fig. 7E-H) correspond to anterior and posterior lens, which appeared to be separated by a compartment boundary: although cells mixed within each domain, there was little or no mixing between them. Cells within each compartment traveled along similar trajectories (Fig. 7N, supplementary material Movie 8), with one exception: during pinwheel movement (12-14 hpf), the posteriormost lens cells stalled or moved anteriorly, initiating posterior lens compaction (data not shown).

Kaede fate mapping confirmed these results ($n=17$). Marking anterior ectoderm (12 hpf) yields the entire anterior lens (24 hpf), with few cells in the posterior half (Fig. 7O, P), which might be due

to imprecise photoactivation without a morphological landmark. Alternately, there might be a little mixing across the AP boundary that was overlooked in our tracking. Non-lens ectoderm remained labeled at 24 hpf (Fig. 7P), indicating that the prospective lens cells at 12 hpf are intermixed with non-lens cells.

Conservation of cell movements among vertebrates

Having mapped cell movements underlying OCM in fish, we asked whether two surprising aspects were evolutionarily conserved: pinwheel movement underlying OV elongation, and the AP division of the lens ectoderm.

In chick, the primary OVs have formed by the seven-somite stage [ss; HH stage 9 (Hamburger and Hamilton, 1992)], and elongate through 19 ss (HH stage 13). The OV elongates laterally, rather than posteriorly as in zebrafish. To test for pinwheel movements, Dil (pseudocolored green) was applied to the OV at either the lateral margin (Fig. 8A) or anterior margin (Fig. 8C, arrowhead). During elongation, each lateral Dil mark (Fig. 8A) swept posteriorly and medially (Fig. 8B; $n=12/12$), while each anterior Dil mark (Fig. 8C, arrowhead) moved laterally (Fig. 8D; $n=10/10$). We conclude that cells are undergoing a stereotyped pinwheel movement like that in zebrafish (Fig. 8E).

Testing for pinwheel movement allowed us to simultaneously test for eye rotation during these early stages. Initially, the Dil labels were located on the lateral OV margin, distributed randomly along the dorsal-ventral axis (Fig. 8A',C'). After elongation, lateral cells had moved dorsally (Fig. 8B'; $n=9/11$), while anterior cells had moved ventrally (Fig. 8D', arrowhead; $n=7/10$). As with zebrafish, the extent of movement varied depending on position. Thus, the chick OV rotates (counterclockwise, left lateral view), as in zebrafish (Fig. 8F).

In chick, the lens placode forms at 20 ss (HH stage 13+) and has invaginated completely by 26–28 ss (HH stage 16). To test for conservation of the lens fate map, Dil was applied to anterior (Fig. 8G; $n=9$) or posterior (Fig. 8I; $n=7$) ectoderm overlying the OV prior to lens placode formation (8 or 10 ss). After OCM, anterior (Fig. 8G) and posterior (Fig. 8I) ectoderm gave rise to distinct lens domains (Fig. 8H,J). Occasionally, some labeling appeared to cross the boundary, probably because no morphological landmark guides initial labeling. We conclude that the lens fate map (Fig. 8K), with its AP boundary, is at least partly conserved between zebrafish and chick.

DISCUSSION

OC morphogenesis generates the fundamental structure of the eye. Here, to probe vertebrate OCM, we used 4D imaging and cell tracking, which present several advantages. First, live analysis eliminates fixation artifacts, yielding more accurate size and shape measurements. Second, tracking many cells from a single dataset allows us to precisely visualize movement of cells relative to one another and within tissue structure. Third, the high temporal resolution of the data allows us to easily discern changes in speed and trajectory. Finally, with these datasets collected, we can ask new questions in the future.

Cell tracking in four dimensions is a difficult computational problem: nuclei are often irregularly shaped, and cells can divide frequently and move quickly. Although advances have been made in automated 4D cell tracking (Bao et al., 2006; England et al., 2006; Fernandez et al., 2010; Keller et al., 2008; McMahon et al., 2008; Megason and Fraser, 2003; Olivier et al., 2010; Rembold et al., 2006), in most cases it is not easy to apply existing algorithms to a given dataset. We therefore used manual tracking with our newly developed tool, LongTracker. Because of the limitations of

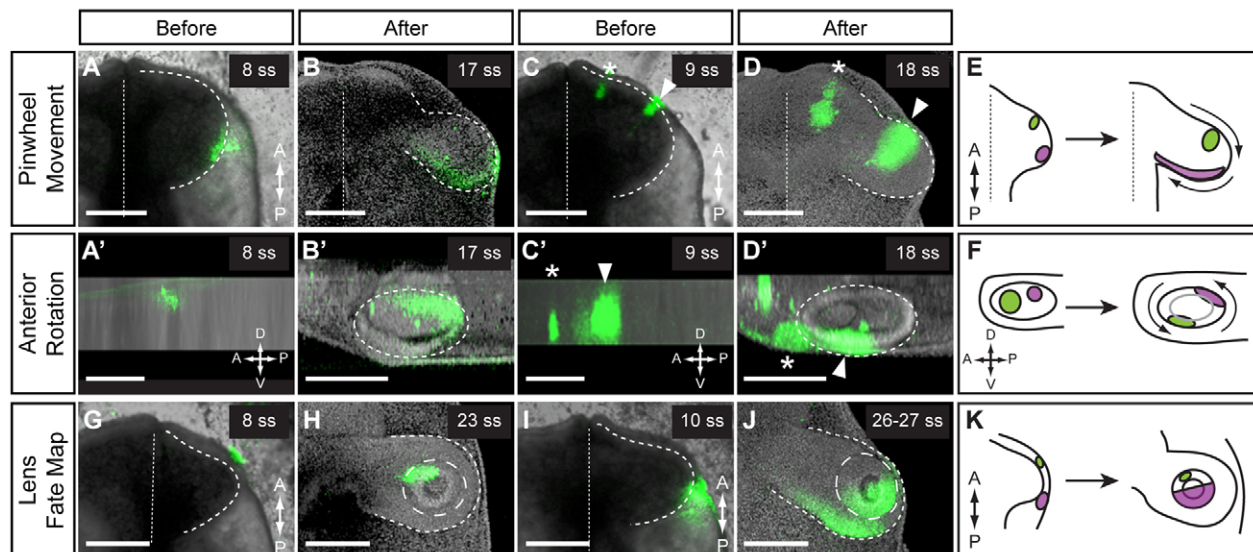


Fig. 8. Conservation of movements in chick OCM. (A–F) Pinwheel movement and anterior rotation. Lateral (A,A') or anterior (C,C') OV was labeled and imaged immediately. (A,C) Ventral views. (A',C') Lateral views. (C) Two anterior Dil spots were marked: medial spot (asterisk), brain; lateral spot (arrowhead), OV. The lateral Dil spot moved medially (B) and dorsally (B'). The anterior Dil spot (arrowhead) moved laterally (D) and ventrally (D'). (B,D) Ventral views. (B',D') Lateral views. Dashed line outlines OV; dotted line indicates the midline. (E) Summary of pinwheel movement. (F) Summary of anterior rotation. (G–K) Lens fate map. Anterior (G) or posterior (I) ectoderm was labeled and imaged immediately. Ventral view. Dashed line outlines OV; dotted line indicates the midline. (H,J) The Dil label was found in distinct lens domains. Ventral view. Dashed line outlines OV; long-dashed line outlines lens. (K) Summary of lens fate map. Volume renderings: Dil and brightfield (A,A',C,C',G,I) or Dil and nuclear counterstain (B,B',D,D',H,J). Scale bars: 200 μ m.

manual tracking, we tracked ~3% of OC cells; development of additional tools will facilitate in toto analysis (Megason and Fraser, 2003).

Cellular basis of OCM

Since proliferation is dispensable for OCM (Fig. 3), we focused on cell movements, mapping for the first time the movements that shape the vertebrate eye. During the first phase of OCM (12–14 hpf), the OV is still undergoing evagination; late-ingressing cells are destined for the ventral retina. Concurrently, all three tissues (NR, RPE, lens) undergo pinwheel movement, which results in OV elongation and optic stalk constriction. During the next phase (14–16 hpf), late evagination ends and cell movements shift: many cells (posterior NR, RPE, lens; central NR, RPE; dorsal NR) turn sharply. During the third phase (16–24 hpf), the OV invaginates: the RPE spreads, lens cells converge, and retinal precursors undergo rim movement, moving from the medial to lateral layer around most of the OV circumference. Concurrent with all of these movements, and spanning the entire 12–24 hpf period, the eye gradually rotates anteriorly in a plane perpendicular to that of pinwheel movement.

OCM is often depicted as a series of differently folded epithelial sheet models. We do not know the extent of epithelial folding here as we have not analyzed cell morphology or single cell behavior. However, previous work suggests that, in fish, single cell migration, rather than the movement of coherent epithelial sheets, drives OV evagination (Rembold et al., 2006). Further work is required to determine the extent to which non-epithelial cell behaviors drive subsequent steps of OCM.

Two previous studies have used in toto imaging to map cell movements during evagination stages (England et al., 2006; Rembold et al., 2006). Our work extends these analyses, beginning after the early evagination stages, by mapping cell movements through the subsequent stages of OCM. It will be interesting to integrate the data and determine whether regional behaviors, including subdomain boundaries, persist from neural plate stages through OC formation. The answers might be informative as to the signals regulating specific cell movements.

Although zebrafish OV evagination was described as complete by 12 hpf (Schmitt and Dowling, 1994), we find that it persists until ~16 hpf. Cells destined for the ventroanterior OC move from brain to eye after 12 hpf (Fig. 2C–F). A similar extended evagination in *Xenopus* (Holt, 1980) suggests evolutionary conservation. A failure to complete this movement might have implications for chorioretinal coloboma, which is characterized by faulty choroid fissure closure. Adding to the mechanisms that might underlie such a defect, we propose a novel one: if late ingression from brain to OV does not occur, the choroid fissure may be left open because its cells never join the eye.

The cellular basis of OV elongation was unknown. Proliferation was controversially proposed to underlie chick OV elongation (Hilfer et al., 1981; Schook, 1980a; Silver, 1981). During zebrafish elongation, we find only a slight posterior bias for mitosis. Rather, cells rapidly move in a coordinated pinwheel pattern (Fig. 4), which is conserved in chick (Fig. 8). Although localized proliferation might still contribute to chick elongation, the pattern of cell movement is clearly conserved.

A surprising aspect of OV elongation is the concurrent movement of lens and retinal precursors, with similar trajectories and velocities (Figs 4, 7, supplementary material Fig. S2). This occurs earlier than any previously described coordination: at later stages of mouse eye development, filopodial contacts between the lens placode and retina coordinate the concurrent invagination of

lens and retina (Chauhan et al., 2009). Our results suggest that these tissue layers are moving in concert at earlier stages, raising the intriguing possibility that coordinated movement enables lens preplacode signaling to NR precursors, which is necessary for later invagination (Hyer et al., 2003).

To our knowledge, rim movement – the involution of cells from the medial to lateral layer around the rim of the invaginating OV (Fig. 4J–M') – has not been described in other vertebrates. We observe cells moving around both anterior and posterior rims; combined with previous observations (Li et al., 2000; Picker et al., 2009), we propose that cells flow around most, or all, of the invaginating OV circumference. In zebrafish, ventral rim movements are influenced by FGF signaling, possibly by controlling epithelial cohesion of prospective anterior retina (Picker et al., 2009); other signaling pathways might coordinate rim movement and epithelial cohesion at other OV locations. Rim movement has implications for cell fate. Although the medial layer is commonly depicted as prospective RPE, our data show that much of it is actually prospective retina. The medial layer may also contribute to the ciliary marginal zone, where retinal stem cells later reside.

Fate maps

Our tracking data allowed us to generate subdomain fate maps, which were confirmed by Kaede fate mapping. Not every cell was tracked, so domain boundaries are somewhat imprecise, especially in the ventral eye, where reduced image quality hindered tracking.

The central retina has not previously been described as a discrete domain; indeed, we added it only after observing the unique gamma-shaped trajectory of the cells. Their distinctly lateral origin might expose these cells to specific ectodermal signals, rendering them competent to propagate the initial wave of retinal ganglion cell differentiation. It was previously shown that initiation of *ath5* (*atox7*) expression occurs in tissue adjacent to the optic stalk (Masai et al., 2000); perhaps the juxtaposition of cells ingressing during late evagination (adjacent to the optic stalk) and central retina demarcates the initial wave of retinal ganglion cell differentiation.

Similar to chick, the zebrafish lens arises from a large ectodermal domain (Fig. 7) (Bhattacharyya et al., 2004). Surprisingly, this domain is subdivided into discrete regions, giving rise to lens domains that comprise functionally distinct cell types (Greiling and Clark, 2009; Lovicu and McAvoy, 2005). We hypothesize that anterior and posterior pre-lens ectoderm are exposed to different signals that initiate distinct differentiation pathways.

Backtracking cell movements allowed us to draw prospective fate boundaries earlier than any known gene expression pattern. For example, we fate mapped the RPE to a small domain at 12 hpf, whereas the first genes specific to the zebrafish RPE, *mitfa* and *mitfb*, are not expressed until ~17 hpf (Lister et al., 2001). Combining gene expression data with our fate maps might suggest the signaling events involved in patterning the OV.

Evolutionary conservation of cell movements

To assess evolutionary conservation, we asked whether chick OV elongation involves pinwheel movements and anterior rotation and if the lens fate map exhibits an AP boundary. As all three answers were affirmative, we propose that the cell movements described here apply generally to vertebrate OCM.

However, there are differences between the chick and fish fate maps. For example, the chick OV posterior margin contributes to ventral OC, whereas in zebrafish it contributes to posterior and

dorsal OC (Fig. 5) (Dutting and Thanos, 1995). How do we reconcile similar morphogenetic movements with fate map differences? Perhaps the same movements are used but to different extents. For example, pinwheel movement appears more dramatic in zebrafish than in chick; consequently, equivalent cells will be adjacent to different tissues and will subsequently encounter different inductive signals. Additionally, patterning signals might act differently between species. For example, FGF signaling in chick and mouse influences retina versus RPE fate (reviewed by Chow and Lang, 2001; Fuhrmann, 2010; Martinez-Morales et al., 2004), whereas in zebrafish it functions in AP retina patterning (Picker and Brand, 2005; Picker et al., 2009).

Conclusions

We combined 4D imaging and custom software to determine the cellular basis of vertebrate eye morphogenesis. This approach can be applied to other morphogenesis events, particularly in zebrafish as a favorable system for 4D imaging. To this end, we plan to make our LongTracker software freely available (H.O., K.R.C., Y. Wan, K.M.K., C. Hansen, C. K. Rodesch and C.-B.C., unpublished). The novel cell movements and fate maps described here represent a significant shift in our comprehension of OCM and should lead to improvements in molecular understanding and models of human eye disease.

Acknowledgements

We thank Takashi Shimada and Kei Ito for use of the cell counting program EVE; the University of Utah Cell Imaging Core and Centralized Zebrafish Animal Resource for support; Sabine Fuhrmann, Kathy Moore, Fabienne Poulain, Melissa Hardy and Charlie Murtaugh for critical reading of the manuscript; and the Chien laboratory for comments and support.

Funding

K.M.K. was supported by a National Institutes of Health (NIH) institutional training grant [5T32 HD07491] and a postdoctoral fellowship from the American Cancer Society [PF-06-146-01-DDC]. H.K. was supported by a grant from the March of Dimes [1-FY08-427 to Y.S.]. This work was supported by grants from the Dana Foundation and the NIH [RO1 EY12873, PO1 HD04886] to C.-B.C. Deposited in PMC for immediate release.

Competing interests statement

The authors declare no competing financial interests.

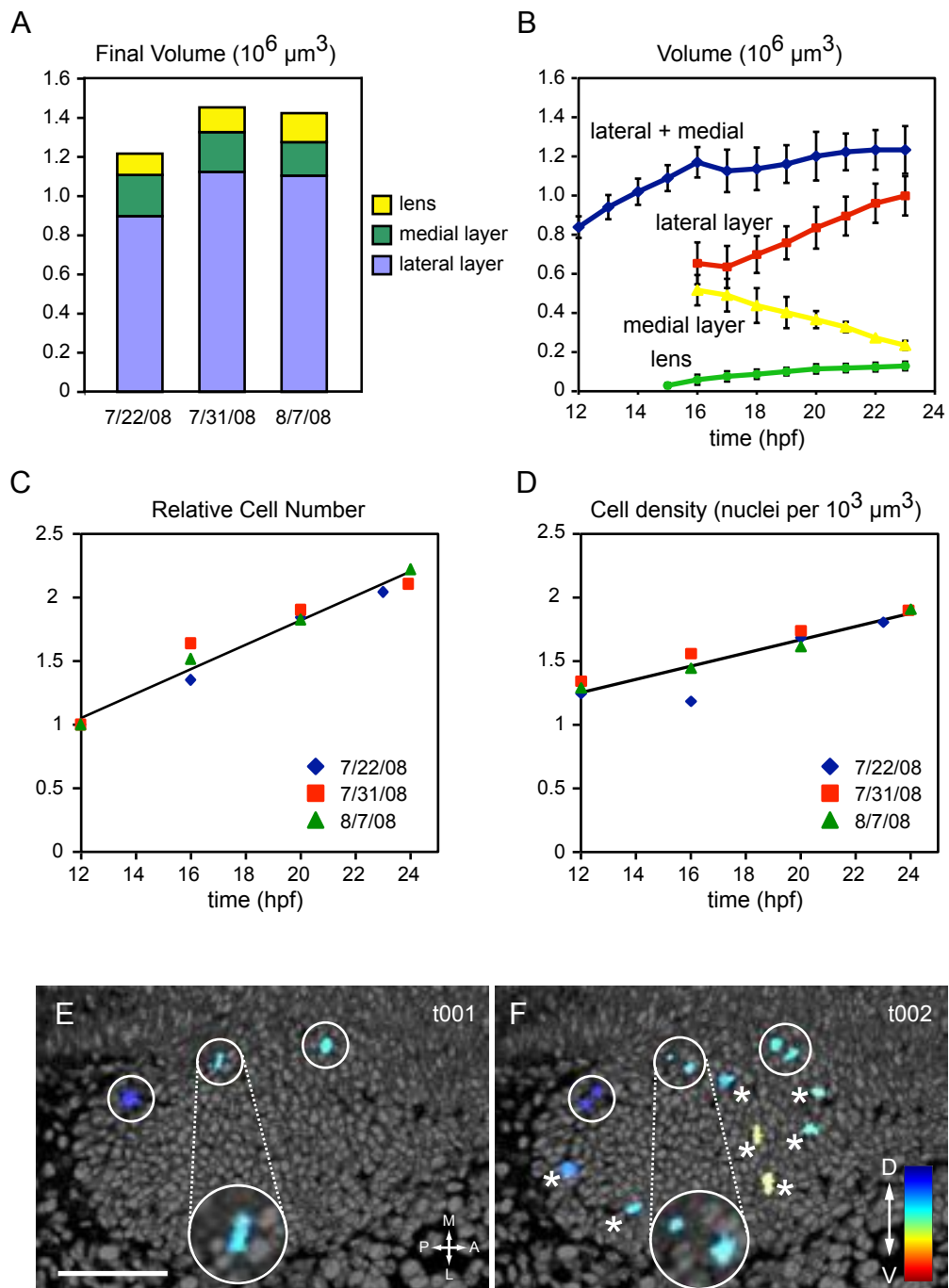
Supplementary material

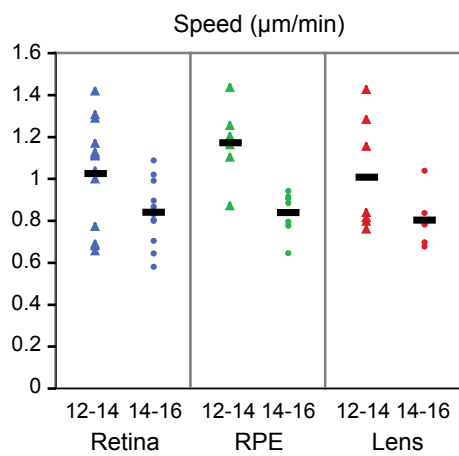
Supplementary material available online at <http://dev.biologists.org/lookup/suppl/doi:10.1242/dev.071407/-/DC1>

References

- Adler, R. and Canto-Soler, M. V. (2007). Molecular mechanisms of optic vesicle development: complexities, ambiguities and controversies. *Dev. Biol.* **305**, 1-13.
- Ando, R., Hama, H., Yamamoto-Hino, M., Mizuno, H. and Miyawaki, A. (2002). An optical marker based on the UV-induced green-to-red photoconversion of a fluorescent protein. *Proc. Natl. Acad. Sci. USA* **99**, 12651-12656.
- Bao, Z., Murray, J. I., Boyle, T., Ooi, S. L., Sandel, M. J. and Waterston, R. H. (2006). Automated cell lineage tracing in *Caenorhabditis elegans*. *Proc. Natl. Acad. Sci. USA* **103**, 2707-2712.
- Bhattacharyya, S., Bailey, A. P., Bronner-Fraser, M. and Streit, A. (2004). Segregation of lens and olfactory precursors from a common territory: cell sorting and reciprocity of *Dlx5* and *Pax6* expression. *Dev. Biol.* **271**, 403-414.
- Brown, K. E., Keller, P. J., Ramialison, M., Rembold, M., Stelzer, E. H., Loosli, F. and Wittbrodt, J. (2010). *Nlcam* modulates midline convergence during anterior neural plate morphogenesis. *Dev. Biol.* **339**, 14-25.
- Chapman, S. C., Collignon, J., Schoenwolf, G. C. and Lumsden, A. (2001). Improved method for chick whole-embryo culture using a filter paper carrier. *Dev. Dyn.* **220**, 284-289.
- Chauhan, B. K., Disanza, A., Choi, S. Y., Faber, S. C., Lou, M., Beggs, H. E., Scita, G., Zheng, Y. and Lang, R. A. (2009). Cdc42- and IRSp53-dependent contractile filopodia tether presumptive lens and retina to coordinate epithelial invagination. *Development* **136**, 3657-3667.
- Chow, R. L. and Lang, R. A. (2001). Early eye development in vertebrates. *Annu. Rev. Cell Dev. Biol.* **17**, 255-296.
- Cole, L. K. and Ross, L. S. (2001). Apoptosis in the developing zebrafish embryo. *Dev. Biol.* **240**, 123-142.
- Dutting, D. and Thanos, S. (1995). Early determination of nasal-temporal retinotopic specificity in the eye anlage of the chick embryo. *Dev. Biol.* **167**, 263-281.
- Eiraku, M., Takata, N., Ishibashi, H., Kawada, M., Sakakura, E., Okuda, S., Sekiguchi, K., Adachi, T. and Sasai, Y. (2011). Self-organizing optic-cup morphogenesis in three-dimensional culture. *Nature* **472**, 51-56.
- England, S. J., Blanchard, G. B., Mahadevan, L. and Adams, R. J. (2006). A dynamic fate map of the forebrain shows how vertebrate eyes form and explains two causes of cyclopia. *Development* **133**, 4613-4617.
- Fernandez, R., Das, P., Mirabet, V., Moscardi, E., Traas, J., Verdeil, J. L., Malandain, G. and Godin, C. (2010). Imaging plant growth in 4D: robust tissue reconstruction and lineaging at cell resolution. *Nat. Methods* **7**, 547-553.
- Fuhrmann, S. (2010). Eye morphogenesis and patterning of the optic vesicle. *Curr. Top. Dev. Biol.* **93**, 61-84.
- Greiling, T. M. and Clark, J. I. (2009). Early lens development in the zebrafish: a three-dimensional time-lapse analysis. *Dev. Dyn.* **238**, 2254-2265.
- Hamburger, V. and Hamilton, H. L. (1992). A series of normal stages in the development of the chick embryo. 1951. *Dev. Dyn.* **195**, 231-272.
- Harris, W. A. and Hartenstein, V. (1991). Neuronal determination without cell division in *Xenopus* embryos. *Neuron* **6**, 499-515.
- Hilfer, S. R. (1983). Development of the eye of the chick embryo. *Scan. Electron Microsc.* **3**, 1353-1369.
- Hilfer, S. R., Brady, R. C. and Yang, J.-J. W. (1981). Intracellular and extracellular changes during early ocular development in the chick embryo. In *Ocular Size and Shape: Regulation During Development* (ed. S. R. Hilfer and J. B. Sheffield), pp. 47-78. New York: Springer-Verlag.
- Holt, C. (1980). Cell movements in *Xenopus* eye development. *Nature* **287**, 850-852.
- Hyer, J., Kuhlman, J., Afif, E. and Mikawa, T. (2003). Optic cup morphogenesis requires pre-lens ectoderm but not lens differentiation. *Dev. Biol.* **259**, 351-363.
- Keller, P. J., Schmidt, A. D., Wittbrodt, J. and Stelzer, E. H. (2008). Reconstruction of zebrafish early embryonic development by scanned light sheet microscopy. *Science* **322**, 1065-1069.
- Kimmel, C. B., Ballard, W. W., Kimmel, S. R., Ullmann, B. and Schilling, T. F. (1995). Stages of embryonic development of the zebrafish. *Dev. Dyn.* **203**, 253-310.
- Kozlowski, D. J., Murakami, T., Ho, R. K. and Weinberg, E. S. (1997). Regional cell movement and tissue patterning in the zebrafish embryo revealed by fate mapping with caged fluorescein. *Biochem. Cell Biol.* **75**, 551-562.
- Laemle, L. K., Puzkarczuk, M. and Feinberg, R. N. (1999). Apoptosis in early ocular morphogenesis in the mouse. *Brain Res. Dev. Brain Res.* **112**, 129-133.
- Lang, R. A. (2004). Pathways regulating lens induction in the mouse. *Int. J. Dev. Biol.* **48**, 783-791.
- Lee, H. Y., Wroblewski, E., Philips, G. T., Stair, C. N., Conley, K., Reedy, M., Mastick, G. S. and Brown, N. L. (2005). Multiple requirements for *Hes 1* during early eye formation. *Dev. Biol.* **284**, 464-478.
- Lee, J., Willer, J. R., Willer, G. B., Smith, K., Gregg, R. G. and Gross, J. M. (2008). Zebrafish blowout provides genetic evidence for Patched1-mediated negative regulation of Hedgehog signaling within the proximal optic vesicle of the vertebrate eye. *Dev. Biol.* **319**, 10-22.
- Li, Z., Joseph, N. M. and Easter, S. S., Jr (2000). The morphogenesis of the zebrafish eye, including a fate map of the optic vesicle. *Dev. Dyn.* **218**, 175-188.
- Lister, J. A., Close, J. and Raible, D. W. (2001). Duplicate *mitf* genes in zebrafish: complementary expression and conservation of melanogenic potential. *Dev. Biol.* **237**, 333-344.
- Lovicu, F. J. and McAvoy, J. W. (2005). Growth factor regulation of lens development. *Dev. Biol.* **280**, 1-14.
- Lupo, G., Gestri, G., O'Brien, M., Denton, R. M., Chandraratna, R. A., Ley, S. V., Harris, W. A. and Wilson, S. W. (2011). Retinoic acid receptor signaling regulates choroid fissure closure through independent mechanisms in the ventral optic cup and periorbital mesenchyme. *Proc. Natl. Acad. Sci. USA* **108**, 8698-8703.
- Lyons, D. A., Pogoda, H. M., Voas, M. G., Woods, I. G., Diamond, B., Nix, R., Arana, N., Jacobs, J. and Talbot, W. S. (2005). *erbb3* and *erbb2* are essential for schwann cell migration and myelination in zebrafish. *Curr. Biol.* **15**, 513-524.
- Martin-Partido, G., Rodriguez-Gallardo, L., Alvarez, I. S. and Navascues, J. (1988). Cell death in the ventral region of the neural retina during the early development of the chick embryo eye. *Anat. Rec.* **222**, 272-281.
- Martinez-Morales, J. R., Rodrigo, I. and Bovolenta, P. (2004). Eye development: a view from the retina pigmented epithelium. *BioEssays* **26**, 766-777.
- Martinez-Morales, J. R., Rembold, M., Greger, K., Simpson, J. C., Brown, K. E., Quiring, R., Pepperkok, R., Martin-Bermudo, M. D., Himmelbauer, H. and Wittbrodt, J. (2009). *ojoplano*-mediated basal constriction is essential for optic cup morphogenesis. *Development* **136**, 2165-2175.

- Masai, I., Stemple, D. L., Okamoto, H. and Wilson, S. W. (2000). Midline signals regulate retinal neurogenesis in zebrafish. *Neuron* **27**, 251-263.
- McMahon, A., Supatto, W., Fraser, S. E. and Stathopoulos, A. (2008). Dynamic analyses of Drosophila gastrulation provide insights into collective cell migration. *Science* **322**, 1546-1550.
- Megason, S. G. and Fraser, S. E. (2003). Digitizing life at the level of the cell: high-performance laser-scanning microscopy and image analysis for in toto imaging of development. *Mech. Dev.* **120**, 1407-1420.
- Mic, F. A., Molotkov, A., Molotkova, N. and Duester, G. (2004). Raldh2 expression in optic vesicle generates a retinoic acid signal needed for invagination of retina during optic cup formation. *Dev. Dyn.* **231**, 270-277.
- Olivier, N., Luengo-Oroz, M. A., Duloquin, L., Faure, E., Savy, T., Veilleux, I., Solinas, X., Debarre, D., Bourguin, P., Santos, A. et al. (2010). Cell lineage reconstruction of early zebrafish embryos using label-free nonlinear microscopy. *Science* **329**, 967-971.
- Picker, A. and Brand, M. (2005). Fgf signals from a novel signaling center determine axial patterning of the prospective neural retina. *Development* **132**, 4951-4962.
- Picker, A., Cavodeassi, F., Machate, A., Bernauer, S., Hans, S., Abe, G., Kawakami, K., Wilson, S. W. and Brand, M. (2009). Dynamic coupling of pattern formation and morphogenesis in the developing vertebrate retina. *PLoS Biol.* **7**, e1000214.
- Pinson, K. I., Brennan, J., Monkley, S., Avery, B. J. and Skarnes, W. C. (2000). An LDL-receptor-related protein mediates Wnt signalling in mice. *Nature* **407**, 535-538.
- Rembold, M., Loosli, F., Adams, R. J. and Wittbrodt, J. (2006). Individual cell migration serves as the driving force for optic vesicle evagination. *Science* **313**, 1130-1134.
- Schmitt, E. A. and Dowling, J. E. (1994). Early eye morphogenesis in the zebrafish, *Brachydanio rerio*. *J. Comp. Neurol.* **344**, 532-542.
- Schook, P. (1980a). A spatial analysis of the localization of cell division and cell death in relationship with the morphogenesis of the chick optic cup. *Acta Morphol. Neerl. Scand.* **18**, 213-229.
- Schook, P. (1980b). Morphogenetic movements during the early development of the chick eye. A light microscopic and spatial reconstructive study. *Acta Morphol. Neerl. Scand.* **18**, 1-30.
- Silver, J. (1981). The role of cell death and related phenomena during formation of the optic pathway. In *Ocular Size and Shape: Regulation During Development* (ed. S. R. Hilfer and J. B. Sheffield), pp. 1-24. New York: Springer-Verlag.
- Silver, J. and Hughes, A. F. (1973). The role of cell death during morphogenesis of the mammalian eye. *J. Morphol.* **140**, 159-170.
- Tomita, K., Ishibashi, M., Nakahara, K., Ang, S. L., Nakanishi, S., Guillemot, F. and Kageyama, R. (1996). Mammalian hairy and Enhancer of split homolog 1 regulates differentiation of retinal neurons and is essential for eye morphogenesis. *Neuron* **16**, 723-734.
- Trousse, F., Esteve, P. and Bovolenta, P. (2001). Bmp4 mediates apoptotic cell death in the developing chick eye. *J. Neurosci.* **21**, 1292-1301.
- Wan, Y., Otsuna, H., Chien, C. B. and Hansen, C. (2009). An interactive visualization tool for multi-channel confocal microscopy data in neurobiology research. *IEEE Trans. Vis. Comput. Graph.* **15**, 1489-1496.
- Woo, K. and Fraser, S. E. (1995). Order and coherence in the fate map of the zebrafish nervous system. *Development* **121**, 2595-2609.
- Zhou, C. J., Molotkov, A., Song, L., Li, Y., Pleasure, D. E., Pleasure, S. J. and Wang, Y. Z. (2008). Ocular coloboma and dorsoventral neuroretinal patterning defects in Lrp6 mutant eyes. *Dev. Dyn.* **237**, 3681-3689.





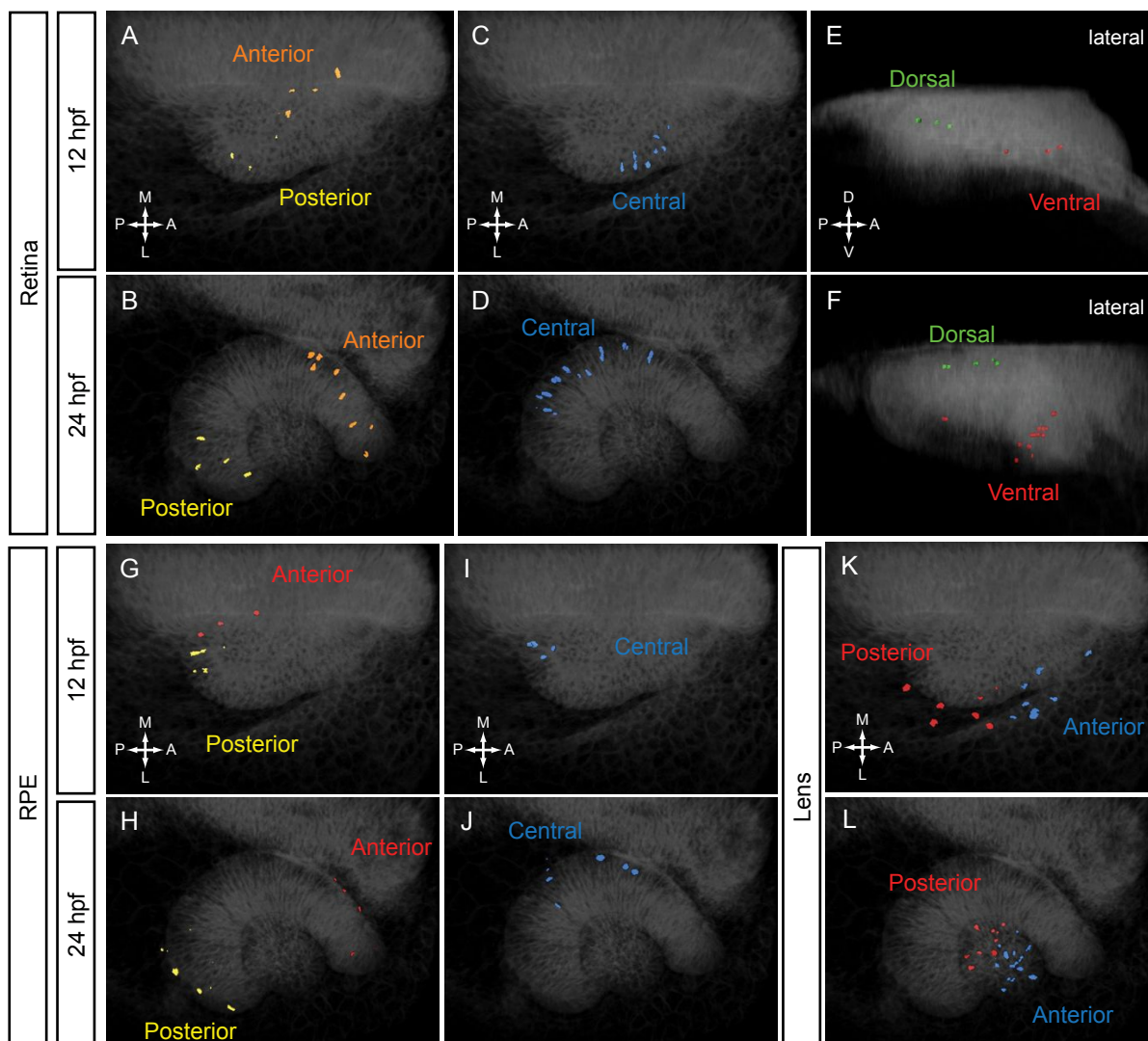


Table S1. Summary of cell tracking

Cell fate	7/31/08	7/22/08	8/7/08	Total
Neural retina	42	13	15	70
RPE	20	9	9	38
Lens	27	5	11	43
Other (optic stalk, mesenchyme)	–	2	–	2
				153

Number of cells tracked for each component tissue from three data sets; 7/31/08 is the primary data set.

Table S2. Summary of cell clustering

	Domain	Cell number
Retina	Anterior	8
	Central	16
	Posterior	4
	Dorsal	5
	Ventral	9
RPE	Anterior	5
	Central	7
	Posterior	8
Lens	Anterior	17
	Posterior	10
Number of cells tracked for each domain from the primary data set (7/31/08) only.		